This document is the accepted manuscript version of the following article:
Cheng, Z. J., Belopolski, I., Tien, H. J., Cochran, T. A., Yang, X. P., Ma, W., … Hasan, M. Z. (2023). Visualization of tunable Weyl line in A-A stacking kagome magnets. Advanced Materials, 35(3), 2205927 (8 pp.).
https://doi.org/10.1002/adma.202205927

Visualization of Tunable Weyl Line in A-A Stacking Kagome Magnets

Zi-Jia Cheng*†1, Ilya Belopolski*1, Hung-Ju Tien*2, Tyler A. Cochran*1, Xian P. Yang*1, Wenlong Ma5, Jia-Xin Yin1, Dong Chen7, Junyi Zhang6, Chris Jozwiak8, Aaron Bostwick8, Eli Rotenberg8, Guangming Cheng9, Md. Shafayat Hossain1, Qi Zhang1, Maksim Litskevich1, Yu-Xiao Jiang1, Nan Yao9, Niels B. M. Schroeter10 ,Vladimir N. Strocov10, Biao Lian6, Claudia Felser9, Guoqing Chang11, Shuang Jia5, Tay-Rong Chang†2,3,4, M. Zahid Hasan†1,12

1. Laboratory for Topological Quantum Matter and Advanced Spectroscopy (B7), Department of Physics, Princeton University, Princeton, NJ, USA
2. Department of Physics, National Cheng Kung University, Tainan, Taiwan
3. Center for Quantum Frontiers of Research and Technology (QFort), Tainan 701, Taiwan
4. Physics Division, National Center for Theoretical Sciences, Taipei, Taiwan
5. International Center for Quantum Materials, School of Physics, Peking University, Beijing, China
6. Department of Physics, Princeton University, Princeton, New Jersey 08544, USA
7. Max Planck Institute for Chemical Physics of Solids, 01187 Dresden, Germany
8. Advanced Light Source, E. O. Lawrence Berkeley National Laboratory, Berkeley, California 94720, USA
9. Princeton Institute for Science and Technology of Materials, Princeton University, Princeton, NJ, USA
10. Swiss Light Source, Paul Scherrer Institute, Villigen 5232, Switzerland
11. Division of Physics and Applied Physics, School of Physical and Mathematical Sciences, Nanyang Technological University, 21 Nanyang Link, 637371, Singapore
12. Lawrence Berkeley National Laboratory, Berkeley, CA 94720, USA

Keywords: Kagome, Weyl semimetal, ARPES, Tunability, Kane-Mele, Spin-Orbit Coupling

Kagome magnets provide a fascinating platform for a plethora of topological quantum phenomena, in which the delicate interplay between frustrated crystal structure, magnetization and spin-orbit coupling (SOC) can engender highly tunable topological states. Here, utilizing angle-resolved photoemission spectroscopy, we directly visualize the Weyl lines with strong out-of-plane dispersion in the A-A stacked kagome magnet $GdMn_6Sn_6$. Remarkably, the Weyl lines exhibit a strong magnetization-direction tunable SOC gap and binding energy tunability after substituting Gd with Tb and Li, respectively. Our results not only illustrate the magnetization direction and valence counting as efficient tuning knobs for realizing and controlling distinct three-dimensional topological phases, but also demonstrate AMn_6Sn_6 (A = rare earth or Li, Mg, Ca) as a versatile material family for exploring diverse emergent topological quantum responses.

† Corresponding authors: zijiac@princeton.edu, u32trc00@phys.ncku.edu.tw, mzhasan@princeton.edu

Topological quantum magnets can host electronic structures with Dirac and Weyl points and lines near the Fermi level, which are effective in concentrating Berry curvature in bulk momentum space [1–7]. This large Berry curvature, in turn, has been observed to drive giant anomalous Hall and Nernst effects [8–14], even up to room temperature [15–17], making these exotic magnets promising candidates for magnetic field sensors [11,18], thermoelectric converters [15,19] and Berry curvature memories [20,21]. Manipulation of the global topology and Berry curvature geometry in such magnetic semimetals promises to enable new exotic responses and device functionality, but remains experimentally challenging. While magnetic topological insulators have long been manipulated by doping and gating to obtain exotic topological states [22–25], known room temperature topological magnetic semimetals are three-dimensional bulk with comparatively high carrier density. The fine tuning of the 3D topological bulk states in those magnetic semimetals is crucial for next-generation topological engineering, but has been little studied or visualized [26,27].

The kagome lattice exhibits frustration and two-dimensional Dirac points, suggesting that stacked kagome materials may naturally promise high tunability of electronic topology with magnetic field or other controllable parameters [6,28–34]. Recently, AMn_6Sn_6 (A is a rare Earth or Li, Mg, Ca) has emerged as a versatile family of kagome magnets offering rich magnetic orders with different cation *A* [35–37], critical temperatures above room temperature and a topological Chern gap arising from a spin-orbit gapped kagome Dirac point [4]. For example, $GdMn_6Sn_6$ is an easy-plane ferrimagnet with a Curie temperature $T_C\sim440$ K [36,38], while $TbMn_6Sn_6$ is an easy-axis ferrimagnet with $T_C\sim 420$ K [36]. Substituting Gd with Tb in alloy $Tb_xGd_{1-x}Mn_6Sn_6$ can further smoothly tune the magnetic ground state without introducing impurity on Mn kagome layer [39], offering an attractive platform for understanding the interplay between magnetic momentum direction and topological electronic structure. Additionally, by replacing the rare earth element with Li, the Fermi level, and thus the energy of the topological features, can also be tuned due to the reduction of the number of valance electrons. Moreover, deviating from ideal quasi-2D kagome model, the low anisotropy in resistivity and highly three-dimensional character of *ab initio* electronic structure calculations [38] suggests a significant interlayer coupling, motivating investigation of three-dimensional topology in AMn_6Sn_6 emerging from the A-A stacked Mn lattice. Here we employ angle-resolved photoemission spectroscopy (ARPES) to probe the three-dimensional electronic structure of $Tb_xGd_{1-x}Mn_6Sn_6$, providing the evidence, for the first time, of three-dimensional magnetic nodal lines with magnetization-direction tunable spin-orbit coupling (SOC) gap. Furthermore, we show that the crossing points of one Weyl line can be tuned extremely close to the Fermi level (E_f) after substituting Gd with Li [Fig.1(d)], which accounts for the enhanced intrinsic AHE in $LiMn_6Sn_6$.

$GdMn_6Sn_6$ has a layered hexagonal crystal structure (P6/mm) [39]. The unit cell exhibits a stacking pattern R-M-S1-S2-S1-M-R along the c direction, where R, M, S1, S2 represent $GdSn_2$ honeycomb layers, Mn kagome layers, Sn hexagonal layers and Sn honeycomb layers, respectively [Fig. 1(a,b)]. The two clean Mn kagome layers in one unit cell form a simple A-A stacking with interlayer separation close to c/2, in sharp contrast to other well-studied kagome magnets such as Fe_3Sn_2 [9], Mn_3Sn [8] and $Co_3Sn_2S_2$ [11]. At low temperatures, $GdMn_6Sn_6$ shows in-plane ferrimagnetic order, but upon substitutional Tb doping ($Tb_{0.2}Gd_{0.8}Mn_6Sn_6$) exhibits a magnetic reorientation transition to an out-of-plane easy axis [Figs. 1(c), S2 [40], [39]].

We first examine our $GdMn_6Sn_6$ samples by high-resolution ARPES on the (001) cleaving plane at incident photon energy 140 eV with linear horizontal (LH) polarization and the results are shown in Figs. 1(e,f). The spectra readily reveal a cone dispersion at the $\overline{K}$ point of the surface Brillouin zone (BZ) with crossing point energy $E_D = -(0.045 \pm 0.01)$ eV and Fermi velocity $v_{KK} = (6.7 \pm 0.8) \times 10^4\ \mathrm{m/s^{-1}}$. This Fermi velocity is significantly smaller than that of graphene, but typical among transition metal kagome magnets [4,29], suggesting a Dirac cone state arising from localized $3d$ electrons on the Mn kagome lattice. As the system is ferrimagnetic, the electronic structure is generically singly- degenerate and these Dirac cones are spin-polarized.

Having observed the Dirac cone state originating from the two-dimensional kagome sheets, we next consider the evolution of this electronic structure in three-dimensional momentum space. We first acquire an ARPES photon energy dependence to probe the electronic structure at different k_z [Fig. 2(a)]. Surprisingly, for the hexagonal state in Fig.1(e) [indicated by the green arrows in Fig.2(a)], we observe a clear oscillation of intensity with a periodicity of $4\pi/c$, doubling the expected $2\pi/c$ periodicity of the nominal bulk BZ. This oscillation indicates a doubling of the effective BZ, or halving of the effective crystallographic unit cell [Fig. 2(b), in the following we will adopt the notation of doubled BZ for the high symmetry points]. To further explore this BZ doubling effect, we examine the electronic structure at $k_z = 9\frac{2\pi}{c}$ ($h\nu = 140$ eV) and $k_z = 10\frac{2\pi}{c}$($h\nu = 172$ eV). In the nominal BZ, these two k_z both correspond to Γ, but now in the doubled BZ they correspond to the Γ-K-M and A_u-H_u-L_u planes, respectively. Zooming in on the Fermi surface (FS) at $k_z = 9\frac{2\pi}{c}$ shown in Fig 2(c), we observe that the upper branch of the Dirac state, labelled D_1, appears as a crescent-moon-shaped pocket centered at H_u. Mimicking graphene [41] and FeSn [29], the observed pattern is consistent with sublattice interference of the lattice-driven nodal state and a manifestation of the π Berry phase of the wavefunction [40,42,43]. In contrast, at $k_z = 10\frac{2\pi}{c}$ the circular Dirac pocket increases in size and its distribution of spectral weight changes dramatically [Fig. 2(f)]. Moreover, the K-K' cut exhibits hole-like linearly dispersing bands [Fig. 2(g)]. The full dispersion is well captured by a fit to a minimal kagome model, which is shown as dashed line in Fig. 2(g), suggesting a kagome Dirac crossing point (label D_2) at 130 meV above E_F. We observe that the Fermi velocity of D_2 is nearly twice that of D_1, indicating distinct Mn orbital origins for the D_1 and D_2 kagome Dirac cones [also see Figs. S7-8]. To understand the interplay between the Mn kagome Dirac cones and doubled BZ, we note that the conventional unit cell contains two Mn kagome planes, with almost equal intra-unit-cell distance (4.51Å) and inter-unit-cell distance (4.49Å), naturally halving the effective crystallographic unit cell [left panel in Fig. 2(b)]. As the states with energy near E_f are mainly from Mn 3d orbitals [Fig. S12 [40]], the observed zone-selective behavior of the states can be understood as an interference effect from the electrons emitting from adjacent kagome planes, which carries phase information of the initial states [40]. We further support this interpretation by band unfolded Green's function *ab initio* calculations, which capture both the observed dispersion and spectral weight distribution of the cones states and the inner hexagonal pocket at alternating n [Figs. 2(e,h), also see Fig.S9 [40]]. The clear BZ doubling with alternating appearance of distinct Dirac states indicates the bulk nature of the kagome Dirac cones, and further points to a significant coupling between Mn kagome layers, suggesting an emergent three-dimensional magnetic topological state.

To probe the evolution of the kagome Dirac states in the stacking direction, we explore our $GdMn_6Sn_6$ samples by bulk sensitive soft-X-ray ARPES(SX-ARPES). We acquire a photon energy dependence to extract the E - k_z dispersion along K-H_u [Fig. 3(a), Fig. S11 [40]], which cuts through the D_1 kagome Dirac cone. Remarkably, we observe a considerable out-of-plane k_z bandwidth of 120 meV for the kagome Dirac state, with the band top at H_u and the band bottom near H. We further acquire conventional ARPES spectra on the (100) side surface to probe more directly, without photon energy dependence, the E - k_z dispersion through D_2 [Fig. 3(b)]. Again we observe a large k_z bandwidth of 230 meV, suggestive of a strongly out-of-plane dispersive kagome Dirac state. The k_z dispersion for both three-dimensional Dirac cone structures quantitatively agrees with our band-unfolded *ab initio* calculations shown in Fig. 3(c) (see Fig.S13 for more details). Our k_z resolved photoemission spectra suggest that under interlayer coupling the D_1 and D_2 kagome Dirac cones independently form emergent three-dimensional magnetic nodal structures with large k_z dispersion.

To further understand the magnetic nodal structure, we examine our *ab initio* calculation along K-H_u without SOC. We find that the two-fold degeneracy of D_1 is preserved along the entire K-H_u path of the bulk BZ, forming a magnetic nodal line structure which can be understood as a natural consequence of the A-A stacking of kagome sheets [inset of Fig. 3(c)]. Including SOC in our calculation, we find that the induced gap remains extremely small, < 0.5 meV, along the full trajectory of the nodal line [Fig. 4(f)]. By contrast, other kagome magnets , such as Fe_3Sn_2 [9] and $TbMn_6Sn_6$ [4], exhibit a moderate SOC gap of ~30 meV. The small SOC gap can be understood as arising from the cooperative interplay between low site symmetry of the Mn atom and in-plane magnetic order. First, the low site symmetry ($C2_V$) lifts the degeneracy of all Mn 3*d* orbitals, suppressing the effect of on-site SOC on the nodal lines by quenching the orbital degree of freedom. Therefore, the strong on-site SOC doesn't directly contribute to the gap at the crossing point. The next leading contribution is the inter-site Kane-Mele coupling, $H_{KM} \propto J_z S_z$, where J_z and S_z are the out-of-plane components of the orbital and spin angular momenta, respectively. However, the Kane-Mele SOC term is strongly suppressed under the in-plane magnetic order of $GdMn_6Sn_6$, resulting in negligible S_z. The interplay of A-A kagome stacking, low site symmetry and in-plane magnetic order naturally produces D1 and D2 nodal lines in $GdMn_6Sn_6$. Furthermore, given the twofold degeneracy of the band crossings, the nodal lines are Weyl lines and thus are sources of strong Berry curvature [5,7].

Having provided evidence for kagome Weyl lines in $GdMn_6Sn_6$, we next explore magnetically tuning this topological electronic structure. We investigate $Tb_{0.2}Gd_{0.8}Mn_6Sn_6$, with out-of-plane magnetic order, by ARPES near H_u. In $GdMn_6Sn_6$, on an E-k_x cut through the D_1 kagome Weyl line, we observe the expected linear dispersion, with one cone branch suppressed due to sublattice interference [Fig. 4(a)]. Interestingly, in contrast to the gapless dispersion in $GdMn_6Sn_6$, the same cut in $Tb_{0.2}Gd_{0.8}Mn_6Sn_6$ exhibits strongly suppressed spectral weight near the crossing point, indicating the existence of a gap [Figs. 4(b)]. We can directly identify the gap on an energy distribution curve (EDC) through H_u for $Tb_{0.2}Gd_{0.8}Mn_6Sn_6$ [Figs. 4(c), S14 [40]]. Fitting by two Lorentzian peaks yields a gap size $\Delta = (25 \pm 6)$ meV, of the same order of magnitude as the kagome Dirac cone gap observed in Fe_3Sn_2 [8]. By contrast, the corresponding EDC for undoped $GdMn_6Sn_6$ is well-fit by a single Lorentzian peak. Corresponding *ab initio* calculations with in-plane magnetic moment exhibit a near-gapless Weyl line [Fig. 4(d)]. While under out-of-plane magnetic order, the Weyl line develops an SOC gap [Fig. 4(e)]. This out-of-plane SOC gap persists along the full Weyl line trajectory, with the largest splitting at H_u [Figs. 4(g)], suggesting enhanced Kane-Mele SOC associated with the out-of-plane magnetic order. Since the kagome Weyl line disperses close to the Fermi level, Berry curvature generated through the Kane-Mele SOC and concentrated along the Weyl line is expected to contribute to an enhanced AHE under out-of-plane magnetism [Fig. S15 [40]]. Taken together, our photoemission spectra and *ab initio* results suggest the observation of a magnetically tunable Kane-Mele SOC gap in a kagome Weyl line.

The Weyl line can also be rigidly shifted in energy by replacing the rare-earth element with Li. The Mn lattice can be effectively hole-doped with missing two electrons per unit cell from Li. Consequently, the electron pocket of the D1 Dirac crossing is substantially reduced in size comparing with $GdMn_6Sn_6$, as shown in the Fermi surface contour of $LiMn_6Sn_6$ [Fig.5(a)]. The energy moment cut across zone corner further visualizes the linear dispersion of the D1 Weyl line [Fig.5(b)], as both upper and lower branch of the Dirac crossing can be observed. The Fermi velocity of the cone is similar to the value of $GdMn_6Sn_6$, while the crossing energy is lifted up by 30meV and reaches $E_D = -(0.015 \pm 0.01)$ eV, which is nearly at the Fermi level [Fig.5(c)]. Interestingly, a significantly enhanced in-plane intrinsic AHE (0.44 e^2/h per Mn layer) was observed in $LiMn_6Sn_6$ [36], comparing with $GdMn_6Sn_6$ (0.14 e^2/h per Mn layer) and $TbMn_6Sn_6$ (0.12 e^2/h per Mn layer) [34]. The enlarged AHE in $LiMn_6Sn_6$ is consistent with the increasing Berry curvature contribution from the gapped D1 Weyl line as it is moved closer to the E_f, which further demonstrates the dominant role of the D1 Weyl line in the topological transport response of AMn_6Sn_6.

In summary, our systematic VUV and SX-Ray ARPES measurements, combined with *ab initio* calculations, reveal the complete band structure of three-dimensional magnetic Weyl lines originating from the A-A stacked Mn kagome lattice in AMn_6Sn_6, which was previously considered to be a quasi-two-dimensional system [4, 34]. The large k_z dispersion of the Weyl lines, comparing with canonical kagome systems Fe_3Sn_2[9] and FeSn [29], suggests the non-negligible interlayer bounding between Mn kagome planes. This strong interlayer interaction should be considered in the understanding of the exotic properties of AMn_6Sn_6, such as Hall and thermoelectric responses. More importantly, by substituting Gd with Tb or Li, we directly visualize, for the first time, the strongly magnetization-direction sensitive Kane-Mele SOC and binding energy tunability of the Weyl lines. Taken together, the tunability not only indicates the crucial contribution of Berry curvature that concentrated along the gapped D1 Weyl line in the anomalous Hall response, but also demonstrates AMn_6Sn_6 as a promising platform for realizing controllable and robust three-dimensional quantum devices. More generally, with more than 80 compounds sharing similar "166" type crystal structure to AMn_6Sn_6, we anticipate a diverse set of tunable Weyl and Dirac nodal states can be attained through rational cation engineering.

Experimental Section:

Ultraviolet ARPES measurements were performed at beamline 5.2 in the Stanford Synchrotron Light Source (SSRL), beamline 7.0.2 in the Advanced Light Source (ALS) and Bloch beamline in the MAX IV. The energy (angle resolution) was better than 20meV (0.2 degree), respectively. Soft X-ray (SX) ARPES data was collected at the ADRESS beamline at Switzerland Light Source (SLS) [44], with 100meV energy resolution at 650eV photon energy. Samples were cleaved and measured between 10K and 20K. The details of sample preparation, TEM, magnetization characterization and calculation can be found in [40].

Reference:

[1] N. P. Armitage, E. J. Mele, and A. Vishwanath, Weyl and Dirac semimetals in three-dimensional solids. Rev. Mod. Phys. **90**, 015001 (2018).

[2] M. Z. Hasan *et al.*, Discovery of Weyl Fermion Semimetals and Topological Fermi Arc States. Annu. Rev. Condens. Matter Phys. **8**, 289 (2017).

[3] D. N. Basov, R. D. Averitt, and D. Hsieh, Towards properties on demand in quantum materials. Nat. Mater. **16**, 1077 (2017).

[4] J.-X. Yin *et al.*, Quantum-limit Chern topological magnetism in $TbMn_6Sn_6$. Nature **583**, 533 (2020).

[5] I. Belopolski *et al.*, Discovery of topological Weyl fermion lines and drumhead surface states in a room temperature magnet. Science **365**, 1278 (2019).

[6] J.-X. Yin *et al.*, Negative flat band magnetism in a spin–orbit-coupled correlated kagome magnet. Nat. Phys. **15**, 443 (2019).

[7] I. Belopolski *et al.*, Observation of a linked-loop quantum state in a topological magnet. Nature **604**, 647 (2022).

[8] K. Kuroda *et al.*, Evidence for magnetic Weyl fermions in a correlated metal. Nat. Mater. **16**, 1090 (2017).

[9] L. Ye *et al.*, Massive Dirac fermions in a ferromagnetic kagome metal. Nature **555**, 638 (2018).

[10] D. S. Sanchez *et al.*, Observation of Weyl fermions in a magnetic non-centrosymmetric crystal. Nat. Commun. **11**, 3356 (2020).

[11] E. Liu *et al.*, Giant anomalous Hall effect in a ferromagnetic kagome-lattice semimetal. Nat. Phys. **14**, 1125 (2018).

[12] D. Xiao, M.-C. Chang, and Q. Niu, Berry phase effects on electronic properties. Rev. Mod. Phys. **82**, 1959 (2010).

[13] M. Ikhlas *et al.*, Large anomalous Nernst effect at room temperature in a chiral antiferromagnet. Nat. Phys. **13**, 1085 (2017).

[14] S. Nakatsuji, N. Kiyohara, and T. Higo, Large anomalous Hall effect in a non-collinear antiferromagnet at room temperature. Nature **527**, 212 (2015).

[15] A. Sakai *et al.*, Giant anomalous Nernst effect and quantum-critical scaling in a ferromagnetic semimetal. Nat. Phys. **14**, 1119 (2018).

[16] X. Li *et al.*, Anomalous Nernst and Righi-Leduc Effects in Mn_3Sn : Berry Curvature and Entropy Flow. Phys. Rev. Lett. **119**, 056601 (2017).

[17] T. Matsuda *et al.*, Room-temperature terahertz anomalous Hall effect in Weyl antiferromagnet Mn_3Sn thin films. Nat. Commun. **11**, 909 (2020).

[18] T. Suzuki *et al.*, Singular angular magnetoresistance in a magnetic nodal semimetal. Science **365**, 377 (2019).

[19] A. Sakai *et al.*, Iron-based binary ferromagnets for transverse thermoelectric conversion. Nature **581**, 53 (2020).

[20] A. Gao *et al.*, Layer Hall effect in a 2D topological axion antiferromagnet. Nature **595**, 521 (2021).

[21] J. Xiao *et al.*, Berry curvature memory through electrically driven stacking transitions. Nat. Phys. **16**, 1028 (2020).

[22] S.-Y. Xu *et al.*, Hedgehog spin texture and Berry's phase tuning in a magnetic topological insulator. Nat. Phys. **8**, 616 (2012).
[23] C.-Z. Chang *et al.*, Experimental Observation of the Quantum Anomalous Hall Effect in a Magnetic Topological Insulator. Science **340**, 167 (2013).
[24] I. Belopolski *et al.*, A novel artificial condensed matter lattice and a new platform for one-dimensional topological phases. Sci. Adv. **3**, e1501692 (2017).
[25] Y. Tokura, K. Yasuda, and A. Tsukazaki, Magnetic topological insulators. Nat. Rev. Phys. **1**, 126 (2019).
[26] S. Nie *et al.*, Magnetic Semimetals and Quantized Anomalous Hall Effect in EuB_6. Phys. Rev. Lett. **124**, 076403 (2020).
[27] A. Biswas *et al.*, Spin-Reorientation-Induced Band Gap in Fe_3Sn_2 : Optical Signatures of Weyl Nodes. Phys. Rev. Lett. **125**, 076403 (2020).
[28] J.-X. Yin *et al.*, Giant and anisotropic many-body spin–orbit tunability in a strongly correlated kagome magnet. Nature **562**, 91 (2018).
[29] M. Kang *et al.*, Dirac fermions and flat bands in the ideal kagome metal FeSn. Nat. Mater. **19**, 163 (2020).
[30] G. Xu, B. Lian, and S.-C. Zhang, Intrinsic Quantum Anomalous Hall Effect in the Kagome Lattice $Cs_2LiMn_3F_{12}$. Phys. Rev. Lett. **115**, 186802 (2015).
[31] S. S. Zhang *et al.*, Many-Body Resonance in a Correlated Topological Kagome Antiferromagnet. Phys. Rev. Lett. **125**, 046401 (2020).
[32] Z. Lin *et al.*, Flatbands and Emergent Ferromagnetic Ordering in Fe_3Sn_2 Kagome Lattices. Phys. Rev. Lett. **121**, 096401 (2018).
[33] Z. Guguchia *et al.*, Tunable anomalous Hall conductivity through volume-wise magnetic competition in a topological kagome magnet. Nat. Commun. **11**, 559 (2020).
[34] Y.-X. Jiang *et al.*, Unconventional chiral charge order in kagome superconductor KV_3Sb_5. Nat. Mater. (2021).
[35] W. Ma *et al.*, Rare Earth Engineering in RMn_6Sn_6 (R = Gd − Tm , Lu) Topological Kagome Magnets. Phys. Rev. Lett. **126**, 246602 (2021).
[36] G. Venturini, B. C. E. Idrissi, and B. Malaman, Magnetic properties of RMn_6Sn_6 (R = Sc, Y, Gd−Tm, Lu) compounds with $HfFe_6Ge_6$ type structure. J. Magn. Magn. Mater. **94**, 35 (1991).
[37] D. Chen *et al.*, Large anomalous Hall effect in the kagome ferromagnet $LiMn_6Sn_6$. Phys. Rev. B **103**, 144410 (2021).
[38] T. Asaba *et al.*, Anomalous Hall effect in the kagome ferrimagnet $GdMn_6Sn_6$. Phys. Rev. B **101**, 174415 (2020).
[39] N. V. Baranov, E. G. Gerasimov, and N. V. Mushnikov, Magnetism of compounds with a layered crystal structure. Phys. Met. Metallogr. **112**, 711 (2011).
[40] See the Supplmental Material for additional information of methods and materials.
[41] E. L. Shirley *et al.*, Brillouin-zone-selection effects in graphite photoelectron angular distributions. Phys. Rev. B **51**, 13614 (1995).
[42] M. Mucha-Kruczyński *et al.*, Characterization of graphene through anisotropy of constant-energy maps in angle-resolved photoemission. Phys. Rev. B **77**, 195403 (2008).
[43] I. Gierz *et al.*, Illuminating the dark corridor in graphene: Polarization dependence of angle-resolved photoemission spectroscopy on graphene. Phys. Rev. B **83**, 121408 (2011).

[44] V. N. Strocov *et al.*, Soft-X-ray ARPES facility at the ADRESS beamline of the SLS: concepts, technical realisation and scientific applications. J. Synchrotron Radiat. **21**, 32 (2014).

Acknowledgements:

The authors thank Jiabin Yu and Yuanfeng Xu for fruitful discussions. The material characterization (ARPES) is supported by the United States Department of Energy (US DOE) under the Basic Energy Sciences program (grant number DOE/BES DE-FG-02-05ER46200). This research used resources of the Advanced Light Source(ALS), a DOE Office of Science User Facility under contract number DE-AC02-05CH11231. Use of the Stanford Synchrotron Radiation Light Source (SSRL), SLAC National Accelerator Laboratory, is supported by the U.S. Department of Energy, Office of Science, Office of Basic Energy Sciences, under contract no. DE-AC02-76SF00515. The authors acknowledge the Paul Scherrer Institut, Villigen, Switzerland for provision of synchrotron radiation beamtime at the ADRESS beamline of the Swiss Light Source. The authors thank Donghui Lu and Makoto Hashimoto at Beamline 5.2 of the SSRL for support. The authors thank C. Polley, J.Adell and B. Thiagarajan at Beamline Bloch of the Max IV, Lund, Sweden for support. The authors also want to thank J. Denlinger at Beamline 4.0.3(MERLIN) of the ALS for support in getting the preliminary data. The authors also acknowledge use of Princeton University's Imaging and Analysis Center, which is partially supported by the Princeton Center for Complex Materials (PCCM), a National Science Foundation (NSF)-MRSEC program (DMR-2011750). I.B. acknowledges the generous support of the Special Postdoctoral Researchers Program, RIKEN during the late stages of this work. T.A.C. acknowledges the support of the National Science Foundation Graduate Research Fellowship Program (DGE-1656466). B.L. is supported by the Alfred P. Sloan Foundation, the National Science Foundation through Princeton University's Materials Research Science and Engineering Center DMR-2011750, and the National Science Foundation under award DMR-2141966. G.C. would like to acknowledge the support of the National Research Foundation, Singapore under its NRF Fellowship Award (NRF-NRFF13-2021-0010) and the Nanyang Assistant Professorship grant from Nanyang Technological University. T.-R.C. was supported by the 2030 Cross-Generation Young Scholars Program from the National Science and Technology Council (NSTC) in Taiwan (MOST111-2628-M-006-003-MY3), National Cheng Kung University (NCKU), Taiwan, and National Center for Theoretical Sciences, Taiwan. This research was supported, in part, by Higher Education Sprout Project, Ministry of Education to the Headquarters of University Advancement at NCKU. The work in Peking University was supported by CAS Interdisciplinary Innovation Team, the strategic Priority Research Program of Chinese Academy of Sciences, Grant No. XDB28000000 and the National Natural Science Foundation of China No. 12141002, No.12225401. N.B.M.S. was patially supported by Microsoft. The work was also supported partially by the European Research Council (ERC Advanced Grant No. 742068 'TOPMAT'), the DFG through SFB 1143 (project ID. 247310070), and the Würzburg-Dresden Cluster of Excellence on Complexity and Topology in Quantum Matter ct.qmat (EXC2147, project ID. 390858490). M.Z.H. acknowledges support from Lawrence Berkeley National Laboratory and the Miller Institute of Basic Research in Science at the University of California, Berkeley in the form of a Visiting Miller Professorship during the early stage of this work.

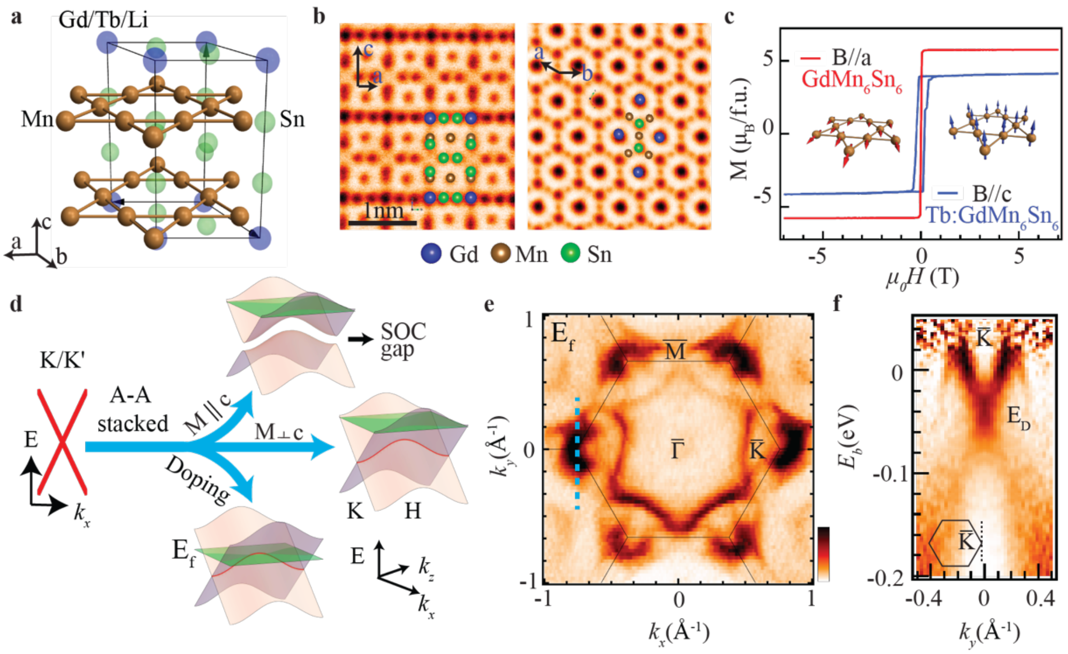

FIG. 1. Structure, magnetism and Dirac crossing in A-A stacking kagome lattice AMn_6Sn_6 (A = Gd,Tb,Li). (a) Crystal structure, emphasizing the A-A stacked Mn kagome lattice. The black lines: side of the conventional unit cell. (b) Scanning transmission electron microscope (STEM) images of side surface (left panel) and top surface (right panel) of $GdMn_6Sn_6$, where the conventional unit cell is superimposed on top of the STEM results. (c) Magnetic moment verses in-plane applied magnetic field (red line, on $GdMn_6Sn_6$) and out-of-plane magnetic field (blue line, $Tb_{0.2}Gd_{0.8}Mn_6Sn_6$ at T = 10 K. f.u.: formula unit. (d) Illustration of the effect of A-A stacking, doping and magnetization direction on the Dirac cone of 2D kagome lattice and the Weyl line along KH direction in 3D kagome magnet. (e) FS map of $GdMn_6Sn_6$ with (001) termination, taken with 140eV, horizontal polarized light and at 16K. The image is obtained by binning within 10meV around the Fermi level. (f) Renormalized ARPES energy-momentum cut along the dashed line in (e).

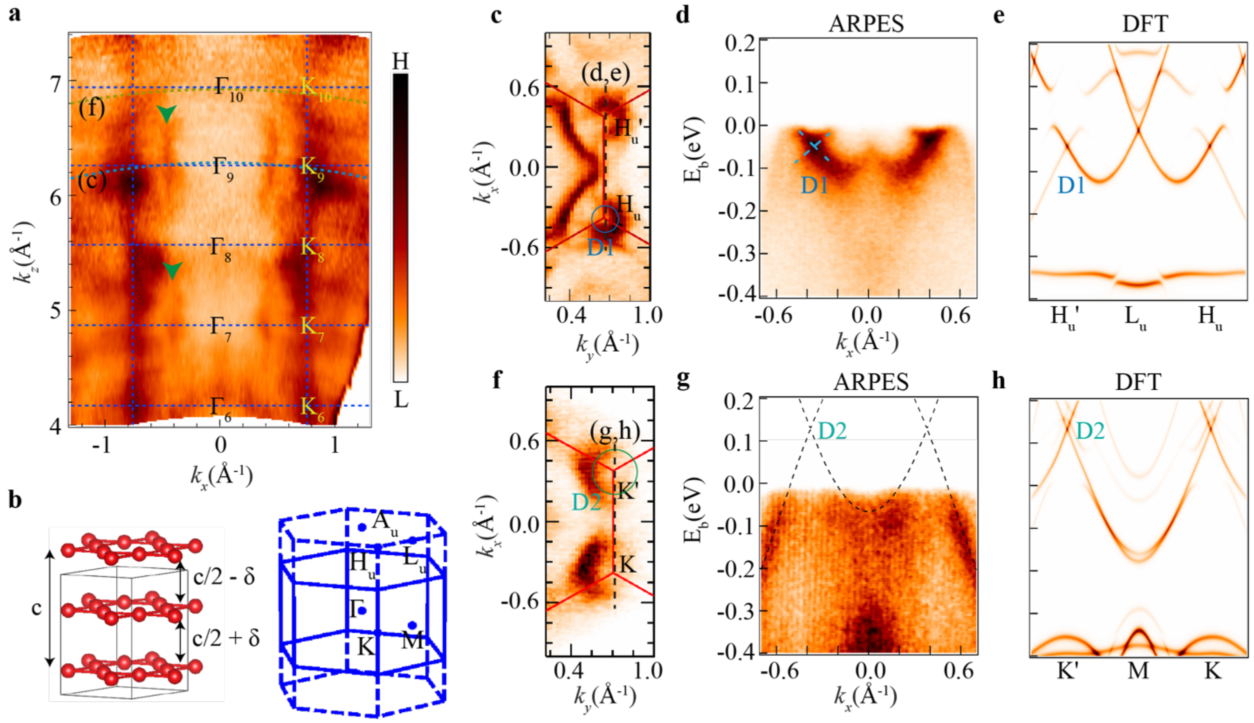

FIG. 2. Photon energy dependence and band unfolding effect of Dirac states. (a) FS map in $k_z - k_x$ plane, showing clear BZ doubling effect of the state marked by the green arrows. Inner potential: $V_0 = 14$ eV. (b) Left: crystal structure with only Mn atoms, which has A-A stacking pattern along c axis with nearly identical interlayer spacing. Right: original BZ (solid line) and doubled BZ (dashed line). (c) and (f) are Fermi surface maps taken at $\mathrm{k_z} \approx 9\frac{2\pi}{c}$ and $\mathrm{k_z} \approx 10\frac{2\pi}{c}$, respectively. The $\mathrm{k_z}$ momentum trajectories of two maps are shown as dashed lines in (a). (d) and (g) are energy-momentum cuts taken along the dashed lines in the corresponding FS maps (c) and (f). The dashed line in (g) is the fitting results using single-orbit kagome model. The two Dirac points are labeled with D1 and D2. (e) and (h) are corresponding theoretical calculations, which shows excellent consistency with (d) and (g), respectively.

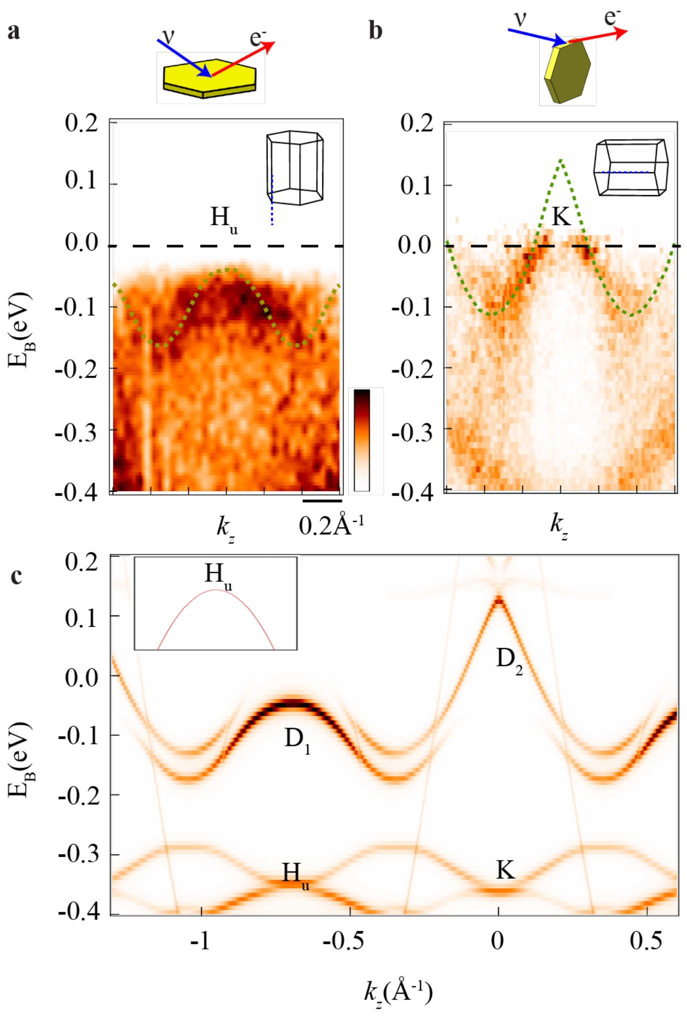

FIG. 3. Strong k_z dispersion of magnetic nodal lines. (a) and (b) are k_z dispersion of the D1 Dirac cones and D2 Dirac cones along K-H direction, respectively. The schematics above the ARPES results show the cleaving plane of each cut. The green dashed lines are the calculation results extracted from (c). (c) The spectrum weight distribution calculated by the unfolded Green's function method. The inset in (c) is the zoom-in theoretical band dispersion (without SOC) of D1 Dirac cones near band top, showing the double degeneracy of the nodal line.

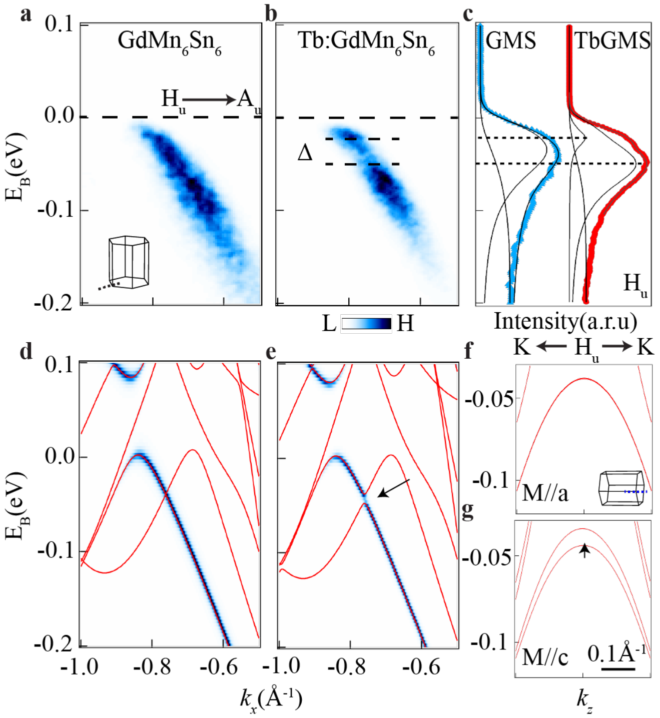

FIG. 4. Magnetic-moment-direction tunable SOC gap of the D1 nodal line. (a) Energy momentum cut along $H_u – A_u$ in the unfolded BZ of $GdMn_6Sn_6$. (b) Analogous to (a), but of $Tb_{0.2}Gd_{0.8}Mn_6Sn_6$. (c) EDCs through the crossing point at H_u (also see Fig. S14). (d-f) Calculated Band dispersion with M//a (d) and M//c (e), for comparison with (a-b). The blue lines are unfolded band calculation. (f-g) Calculated Band dispersion along H_u-K with M//a (f) and M//c (g). The insets in (a) and (g) denote the direction of the cuts in the unfolded BZ.

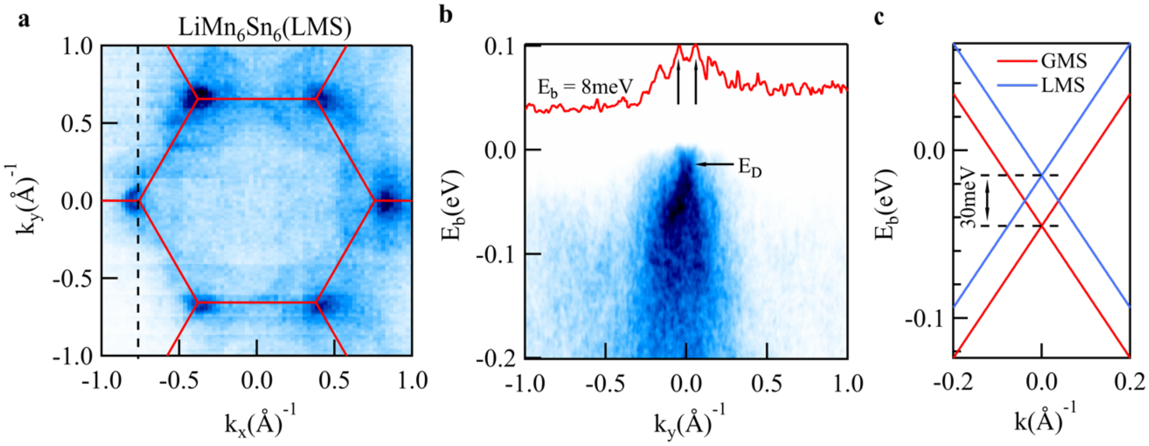

FIG.5. Binding-energy tuning of the Weyl line in a hole-doped Kagome lattice. (a) FS map of LiMn$_6$Sn$_6$ at $k_z = 9\frac{2\pi}{c}$ (Fig.S16), measured with linear horizontal polarized light. (b) Energy-momentum cut along the momentum path indicated by the back dashed line in (a), showing the crossing of the D1 Weyl line. The momentum distribution curve (MDC) at 8meV binding energy is shown as a red line and the two peaks of the upper branch of the crossing are marked by black arrows, respectively. (c) Schematic of the Weyl cone's in-plane dispersion in LiMn$_6$Sn$_6$ (LMS, blue line) and GdMn$_6$Sn$_6$ (GMS, red line).